JOURNAL OF AIRCRAFT
Vol. 44, No. 4, July–August 2007

Design and Testing of a Pneumatic Telescopic Wing for Unmanned Aerial Vehicles

Julie Blondeau Samuel and Darryll Pines
University of Maryland, College Park, Maryland 20742

DOI: 10.2514/1.22205

This paper discusses the design, development, and testing of an unmanned aerial vehicle pneumatic telescopic wing that permits a change in the wingspan, while simultaneously supporting structural wing loads. The key element of the wing is a pressurized telescopic spar able to undergo large-scale spanwise changes while supporting wing loadings in excess of 15 lb/ft^2. The wing cross section is maintained by NACA 0013 rib sections fixed at the end of each element of the telescopic spar. Hollow fiberglass shells are used to preserve the spanwise airfoil geometry and ensure compact storage and deployment of the telescopic wing. A full-scale telescopic wing assembly was built and tested in the Glenn L. Martin Wind Tunnel at the University of Maryland. These tests included aerodynamic measurements at a variety of Reynolds numbers. The telescopic wing was tested in three different configurations and experimental results are compared with finite wing theory and results obtained on a rigid fixed-wing counterpart. Preliminary aerodynamic results were promising for the variable wingspan telescopic wing. As expected, the telescopic wing at maximum deployment incurred a slightly larger drag penalty and a reduced lift-to-drag ratio when compared to its solid fixed-wing counterpart. However, the penalty was minimal and thus the development of an unmanned aerial vehicle with a pneumatic variable span wing is feasible.

Nomenclature

A_p	=	piston area, ft^2
AR	=	aspect ratio
a	=	lift curve slope, deg or rad
a_0	=	theoretical lift curve slope, deg or rad
b	=	wingspan, ft
C_D	=	drag coefficient
$C_{D,i}$	=	induced drag coefficient
C_L	=	lift coefficient
C_0	=	frictional losses coefficient
c	=	chord, ft
D	=	drag force, lb/ft^2
E	=	endurance, h or min
e	=	Oswald factor
F_b	=	friction force, lb/ft^2
I	=	moment of inertia, in.^{4}
L	=	lift force, lb/ft^2
M	=	bending moment, lb/ft
m	=	mass, lb
P	=	pressure force, lb/ft^2
R	=	range, miles or km
S	=	wing reference surface area, ft^2
V	=	shear force, lb
V_∞	=	wind velocity, mph or ft/s
α	=	angle of attack, deg
Γ	=	circulation
Λ	=	sweep angle, deg
ρ	=	air density, slug/ft^3
σ	=	flexural stress, lb/ft^2

I. Introduction

IN THE United States over the past 20 years, research on fixed-wing unmanned air vehicles (UAVs) has been spearheaded by the Defense Advanced Research Projects Agency (DARPA) , the U.S. Air Force, Navy, Army, and Defense Airborne Reconnaissance Office (DARO) [1]. These activities have the goal of achieving a variety of military objectives to aid the "war fighter" in the air, over land, and above the sea. Toward this goal, the Department of Defense (DoD) has fielded numerous vehicle configurations to meet various mission objectives including reconnaissance, surveillance, target acquisition, and search and rescue. Most common vehicles span a three-order of magnitude range in wingspan and a six-order of magnitude range in gross takeoff weight (GTOW).* However, the majority of fixed-wing aircraft have wingspans in the range between 5 and 30 ft with gross takeoff weights varying from approximately 10 to 2000 lb. These vehicles are typically designed to achieve a single mission objective such as reconnaissance, surveillance, or combat. Although many of the current operational platforms have given the war fighter an advantage in the military battlefield, the full potential of UAVs is still emerging, as evidenced by the success of Predator and Global Hawk in the Afghanistan and Iraq conflicts.

New tactical advantages provided by UAVs include situational awareness, standoff weaponry, forward pass targeting, and logistic support. It is anticipated that such autonomous agents will contribute to a new age in war fighting for today's military. In the future, vehicles may be required to achieve multiple mission objectives in a single platform. To enable this capability, the concept of variable geometry has been proposed as a means to extend the capability of current air vehicle platforms. This requires the development of seamless aerodynamic structures that can undergo large-scale changes in wing geometry. In addition, such vehicles must have adaptive control architectures to maintain robust stability and control capability over an expanded flight regime. This should also be achieved without increasing GTOW and altering the ability to sustain aerodynamic loads, operating with efficient propulsion system over an expanded flight envelope.

In spite of the apparent complexity of variable geometry aircraft, nature has evolved thousands of flying machines (insects and birds of prey) that perform far more difficult missions routinely. Thus, biomimetic "morphing" flight may offer many advantages over traditional uninhabited air vehicles [MAVs (micro air vehicle), UAVs, UCAVs (unmanned combat air vehicle), etc.] such as the capability of a seamless morphing air vehicle to transform itself into multiple geometries, enabling multiple mission objectives with one

Received 17 February 2006; accepted for publication 2 January 2007.

*Data available online at http://www.wff.nasa.gov /~apb [retrieved May 2004].

vehicle, thanks to its capability to adapt its shape and power precisely to the flight condition requirements.

In response to the need of such revolutionary aircraft, the Aerospace Department at the University of Maryland initiated in 2002 a threefold Morphing Aircraft research project including camber morphing, sweep morphing, and wingspan morphing concepts. Variation of camber can be used not only to steer an airplane, but also to improve its flying capabilities at specific times by directly influencing the amount of lift and drag produced on an airfoil. Variation of sweep allows not only for stability control, but also control over Mach number in subsonic flight and over the wave drag in supersonic flight. Finally, variation of wingspan affects directly the amount of lift produced on the wing and could provide an alternative form of roll control by means of differential lift. In a conventional wing configuration, roll control is achieved by the use of ailerons, deflected such that lift is increased on one wing and decreased on the other, thus creating a roll moment. In the case of a morphing aircraft, the same roll control can be achieved without ailerons when a span difference is created between the two half wings, yielding a lift differential resulting in a roll moment. In addition, whereas wings with large spans have good range and fuel efficiency but lack maneuverability and have relatively low cruise speeds, aircraft with short, stubby wings are faster and highly maneuverable but show poor aerodynamic efficiency. A variable span wing could integrate into a single aircraft the advantages of both designs. However, although one could expect that endurance and range of an aircraft could be increased by actively adapting the geometry of the wing to the mission profile, weight penalties might be incurred because of additional mechanical components required to achieve morphing.

Telescopic wing technologies [2,3] such as Telescopic Wing Tips or Convertible Fixed Wing were proposed as early as the 1940s but there is little evidence that those early designs were ever built, or flown. More recently, in 1997, Gevers Aircraft, Inc., developed a six-seat "triphibious" aircraft designed for unprecedented speed, utility, safety, and ruggedness. It uses a telescopic wing to adapt the aircraft geometry to the flight conditions. The wing is designed for high-speed cruise when retracted and enhanced low-speed capabilities when extended. It is composed of a fixed center section and two extendable outer sections, using an overlapping extension spar system. The center section is a high-speed wing (low drag and strong) and the completely retractable high-lift section moves in a spanwise direction. It appears that the aircraft actually flew, but no flight test data could be found.[†] Morphing wingspan UAVs have also been developed, such as the Rigidizable Wing [4] developed by the Delaware-based company ILC Dover.

The telescoping wing developed at the University of Maryland explores the idea of using variable span wing morphing to increase aircraft maneuverability, maximize aerodynamic performance for a given mission profile, and possibly act as an effecter of roll control for UAVs. Our work is restricted small UAVs with 8–12 ft wingspans in fully extended configuration. Based on performance enhancements achieved using a variable wingspan, this paper describes the design, development, and wind-tunnel testing of a telescopic wing actuated by pneumatic pressure. Although there are numerous ways to achieve a telescopic wing, including a variety of lead screw or multiple actuator linkage systems, pneumatic pressure appears to offer a practical approach with minimal weight penalty and few moving parts.

II. Pneumatic Telescopic Wing Design and Manufacturing

The primary elements of the pneumatic telescopic wing include one or several actuator(s) to perform the change in wingspan and its control system, a system of structural elements to sustain the aerodynamic loads on the wing, and a type of skin that allows the geometric transformation while maintaining the airfoil shape and permitting the transfer of the aerodynamic loads to the structural elements. Considering these general requirements, a basic design, presented in Fig. 1 in three different stages of extension, with and without the skin, was developed for the telescopic morphing wingspan wing. It is composed of 1) pneumatic telescopic spars and an extension/retraction control mechanism, 2) length sensors embedded in the wing, 3) ribs fixed at the end of each section of the pneumatic telescopic spar, 4) telescopic skin sections that can be adapted to be seamless, and 5) a source of pressurized gas.

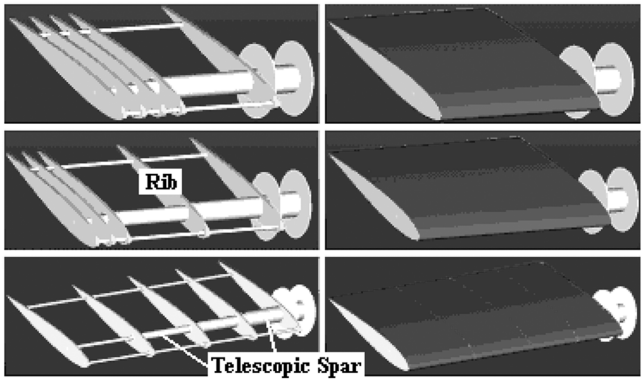

Fig. 1 Conceptual drawings of the pneumatic telescopic wing.

A. Actuator Design and Operation

An important challenge in achieving a variable wingspan wing is to avoid heavy and bulky rack/pinion or cable/pulley systems that were described in previous morphing wingspan concepts. After careful and exhaustive track studies, comparing weight, volume, size, and power requirements, a pneumatic spar configuration appeared to offer the best solution for telescopic deployment. The telescopic spar design consists of concentric circular tubes of decreasing diameter and increasing length, ended by pistons that deploy under pressure to produce various wingspan configurations. The telescopic elements are linked by linear bearings to avoid misalignment and sealed to maintain a constant pressure in operation. The sealed pistons, located at the root of each moving element of the spar, provide the necessary surface area for the pressure force to be applied to move the free tubes with respect to the outer ones.

Several actuator and telescopic wing designs [5–7] of various sizes, and several skin designs were developed and tested. Preliminary experimental investigations suggested that the design of the spars had to be reconsidered for the wing to handle the aerodynamic loads, especially in the dynamic case. In addition, the manufacturing of the spars had to be greatly improved in terms of airtightness to minimize the amount of gas required to operate the spars. Wing twist and fluttering cannot be avoided if only one actuator is used in the wing because the cylindrical elements that compose the spar are free to rotate with respect to each other. Finally, a rigorous and reliable manufacturing process needs to be developed to construct the telescopic skins elements.

As a result of these observations, a different and more robust design was adopted, which consists of two telescopic spars mechanically coupled and used side by side to prevent uncontrolled twisting of the wing and provide more strength and actuation force to the wing. Because of the loading requirements, the actuators are rather bulky, which presents a challenge for the general design of the wing because both actuators had to fit inside the wing. The pneumatic telescopic spars were redesigned, and manufactured by a subcontractor (The Ergo-Help Company, Arlington Heights, Illinois) specializing in high-lift pneumatic telescopic tubes. Figure 2 presents the design adopted.

Figure 3 presents details of the extension and retraction mechanism for the Pneumatic Telescopic Spar. In extension, a pressure input (location 1) at the root (Fig. 3) generates motion of the two mobile sections (locations 2 and 3) with pressure applied on both

[†]Data available online at http://www.geversaircraft.com [retrieved May 2004].

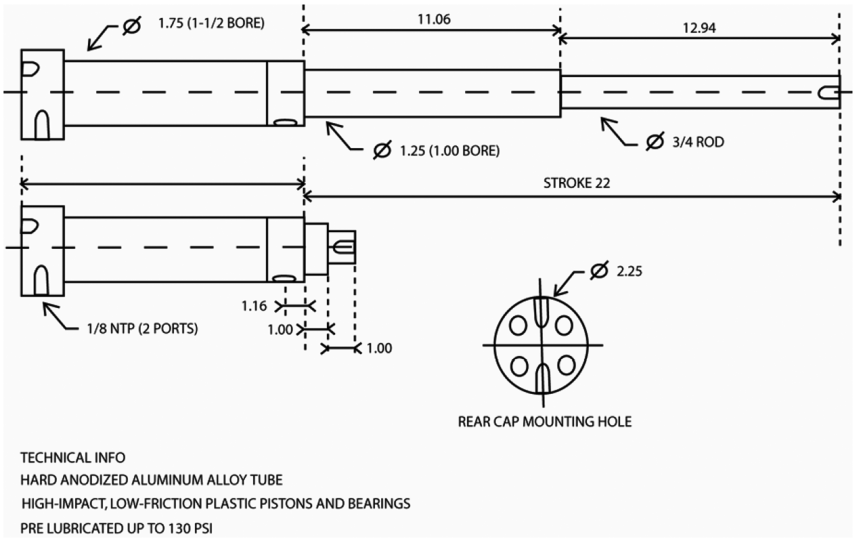

Fig. 2 Pneumatic telescopic spar dimensions.

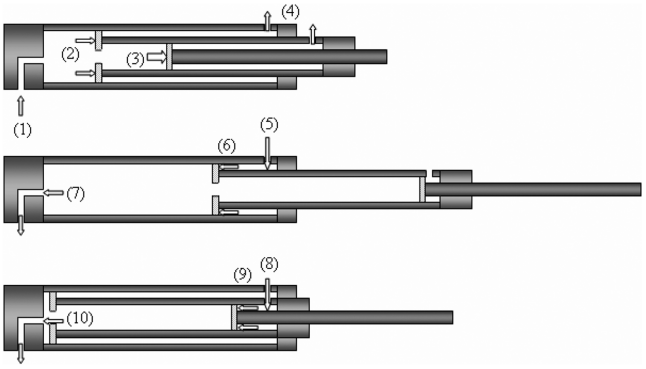

Fig. 3 Pneumatic telescopic spar functional design and operation.

pistons. As a result of the motion, air is exhausted behind the two pistons (Fig. 3) at locations 4 and 5 of Fig. 3. The input and output of pressure orifices are maintained closed (by the solenoid valves) when they are not being used. Hence, the spar is sealed under pressure at every time.

The retraction scheme is slightly different because the pneumatic telescopic spar has only one, fixed, input of pressure to generate the retraction of the spar. Although pressurized gas is input in location 5 (Fig. 3), the retraction of the middle element of the telescopic spar is initiated by the reverse pressure on the piston at location 6 (Fig. 3) and exhaust of pressure at the root of the spar (Fig. 3) at location 7. On the other hand, the tip element of the telescopic spar does not move until the middle element is completely retracted. When this occurs, the middle element is retracted completely; orifices at the tip of the middle element allow the air to push the small piston and initiate retraction of the tip telescopic element.

Therefore, actuation of the span resumes in an input of pressure in location 1 (Fig. 3) for extension associated with opening of orifices at location 4 (Fig. 3) for the extension, and an input of pressure in locations 5 and 8 for extension associated with opening of orifices at locations 7 and 10 for the extension.

As mentioned, a strong design requires two pneumatic telescopic spars to actuate the prototype and support the aerodynamic load on the wing. The two identical spars are placed side by side. They are mechanically coupled by the ribs at the root and at the tip of each section, and receive the same actuation pressures. The design of the ribs will be discussed in further section.

B. Experimental Characterization of Actuator Dynamics

The spars were tested under different loading conditions to characterize their dynamic behavior. The spars were placed

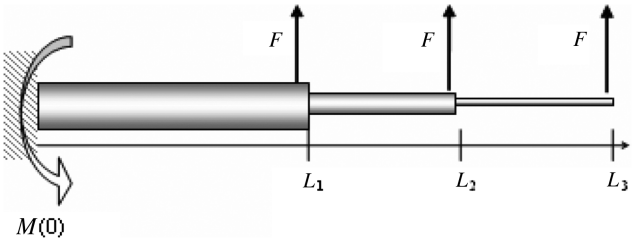

Fig. 4 Experimental/simulation loading.

horizontally, side by side and mechanically coupled, clamped at the root, and the loading was applied upwards to mimic the actual wing configuration. A point force was applied at the tip of each element of the spars as described in Fig. 4. This approach was used to simulate the load on the spar, because each wing section is attached to the spar with a single rib located at the tip of each spar element. In addition, the use of a more distributed load was not feasible because it would interfere with the retraction of the spar elements.

To avoid the inertia effects, the weights used to apply the force F were mounted at the end of cables through pulleys, and placed 10 ft away from the spars. This large distance allows the spar elements to move in the horizontal plane while minimizing the weights' vertical displacement. Thus, the spar elements in motion experience the load without lifting or accelerating the weights. The varying wingspan (extension and retraction) was measured using a potentiometer and wheel system, mounted in alignment with the spars. This experiment was performed at three different pressures (30, 40, and 50 psi) and in three different loading cases (No load, load A, load B).

To define the experimental/simulation required loading cases A and B, the moment over the wing had to be calculated by integrating the lift distribution. The lift force over a rectangular wing can be modeled by Prantl's lifting-line theory [8] using the expression of circulation for an elliptical lift distribution (it is the case for a rectangular wing).

Circulation distribution:

$$\Gamma(x) = \Gamma_o \sqrt{1 - (2x/b)^2} \tag{1}$$

Maximum circulation:

$$\Gamma_o = bV_\infty \alpha(\pi/180) \tag{2}$$

Local lift distribution:

$$L_l(x) = \rho_\infty V_\infty \Gamma(x) \tag{3}$$

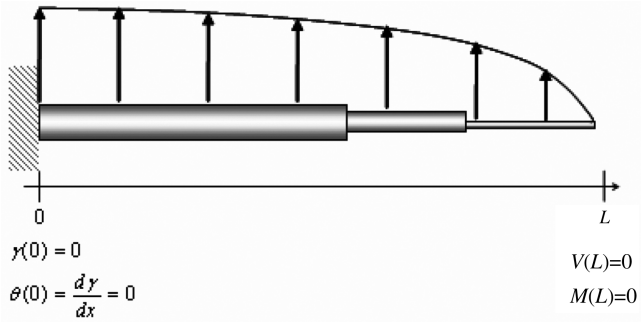

Fig. 5 Elliptical distribution of aerodynamic load on the spars.

Shear and moment:

$$\mathrm{d}V/\mathrm{d}x = -L(x) \quad \text{and} \quad \mathrm{d}M/\mathrm{d}x = V(x) \tag{4}$$

Constants:

$$C_1 = \rho_\infty V_\infty \Gamma_o \quad \text{and} \quad C_2 = 4/b^2 \tag{5}$$

$$a = 1/\sqrt{C_2} \quad \text{and} \quad b = 2L \tag{6}$$

Integration of the lift distribution over the span of the telescopic wing yields an expression for the maximum bending stress at the root of the wing. This is based upon with the values of angle of attack and cruise speed mentioned earlier and in the most critical case (L is the maximum length $L = 38$ in.). Calculations were made for a flight conditions of $\alpha = 6$ deg and $V_\infty = 30$ mph $= 44$ ft/s. These values were chosen because they are at the high end of the operating range for the telescopic wing:

$$M(0) = \frac{C_1\sqrt{C_2}}{2}\frac{(a^2)^{\frac{3}{2}}}{3} + \frac{C_1\sqrt{C_2}}{2}[-(a^2 - L^2)^{\frac{3}{2}}] + \frac{C_1\sqrt{C_2}a^2}{2}\left[a\,\ell_n\left(\tan\frac{L}{2a}\right)\right] + LC_1\sqrt{C_2}\left[\frac{L}{2}\sqrt{a^2 - L^2} + \frac{a^2}{2}\sin^{-1}\left(\frac{L}{a}\right)\right] = 10.3 \text{ lbf} \cdot \text{ft} \tag{7}$$

As described previously, the bending moment at the root was experimentally simulated using three equal weights distributed as the tips of the spar elements. From Fig. 5, the root bending moment is

$$M_{\text{distributed}}(0) = F(L_1 + L_2 + L_3) = M(0)_{\text{elliptical Loading}} \tag{8}$$

The most critical case is when the spar is completely extended as this corresponds to the highest root moment, therefore L_1, L_2, and L_3 were chosen at their highest value: $L_1 = 16.5$ in., $L_2 = 27.5$ in., $L_3 = 38$ in.. The force derived from Eq. (8) is $F = 1.5$ lb. The experimental loading case A was picked such that it is slightly superior to the high operating condition described earlier ($\alpha = 6$ deg and $V_\infty = 30$ mph), with $F_A = 1.58$ lb. Loading case B was chosen

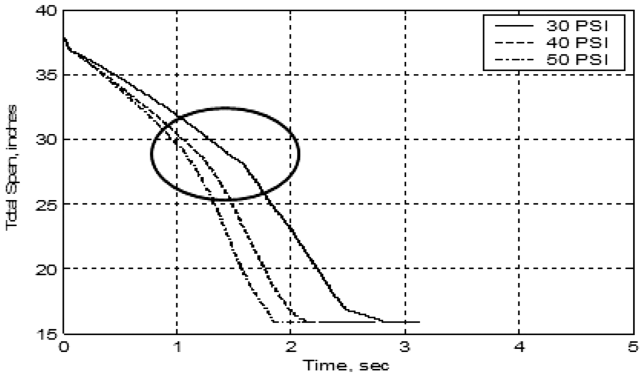

Fig. 6 Retraction of the spars; no load.

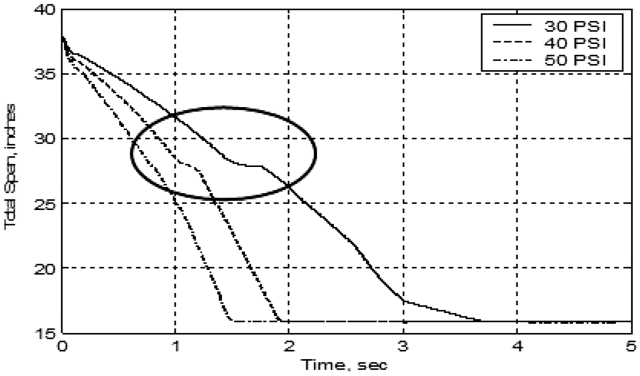

Fig. 7 Retraction of the spars; load A: $F = 1.6$ lb.

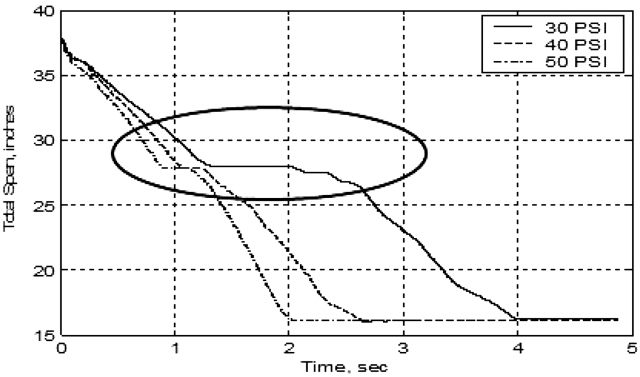

Fig. 8 Retraction of the spars; load B: $F = 2.7$ lb.

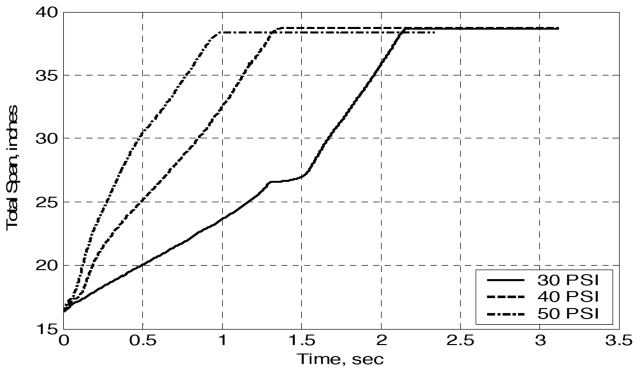

Fig. 9 Extension of the spars; no load.

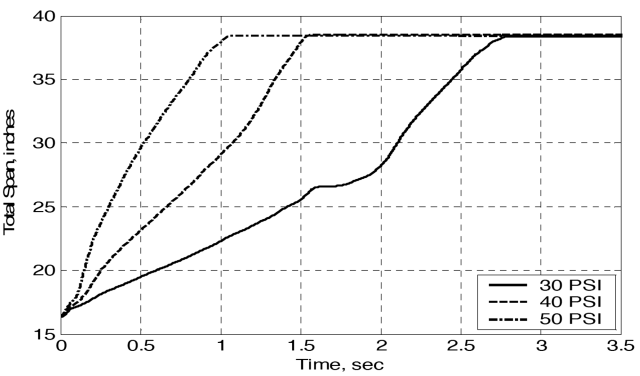

Fig. 10 Extension of the spars; load A: $F = 1.6$ lb.

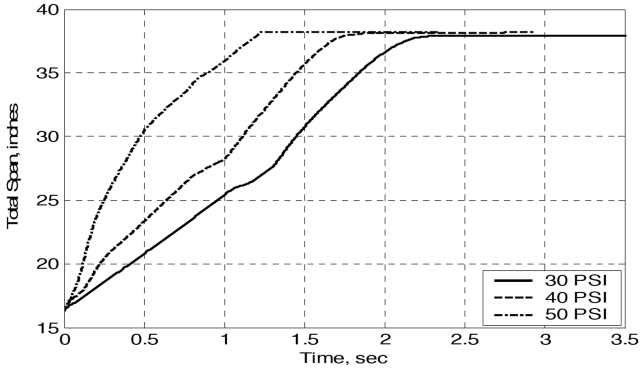

Fig. 11 Extension of the spars; load B: $F = 2.7$ lb.

to be significantly higher than the loading case A, with $F_B = 2.68$ lb. Figures 6–8, and Figs. 9–11, respectively, display the measured span of the spars in retraction and extension, at the three different operating pressures and for the three different loading cases. Each test was repeated five times and the plots are averages of all the tests. Nominal standard deviation for these tests is about 0.85, which shows the good repeatability of the motion.

Several expected behaviors can be observed in both extension and retraction cases:

1) The higher the pressure, the faster the motion.

2) The higher the load, the slower the motion.

In the extension experiments, a sudden change in curve slope can be observed. Before this change occurs, both the middle section and the tip section of the spar are in motion. After that break, the slope decreases because it corresponds to the motion of the tip section of the spars only.

In the retraction experiments, however, as the spar design forces a sequential retraction, the middle section of the spars retracts, then only the tip section of the spars retracts, creating a change in slope. A comparison of Figs. 8–10 shows that the break observed is longer when the load increases and shorter when the pressure increases. This is partly explained by a phenomenon of static friction (stiction) observed when the load bends the spars. The higher the bending load, the higher the force necessary to overcome the stiction. Note that in loading case B, a pressure of 30 psi is barely sufficient to overcome the stiction. The same phenomenon of stiction is observed at the very beginning of the retraction and followed by a short steep slope. Close examination of Figs. 11–13 shows an anomaly that could not be explained: in every case, when the load is increased, the time required to complete extension is also increased and the break in curve slope is more pronounced, except in the case of load B: 30 psi. Experiments were performed several times and the result was consistent. The phenomenon of stiction that was observed during this simulation of the loading likely explains why it was difficult to actuate the wing in the wind in later wind-tunnel tests, in addition to the fact that the bending of the skin causes friction.

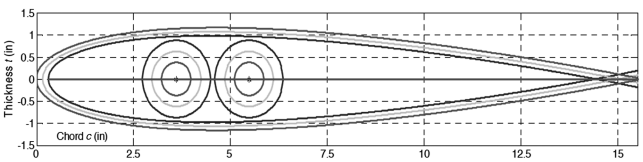

Fig. 12 Telescopic wing airfoil design.

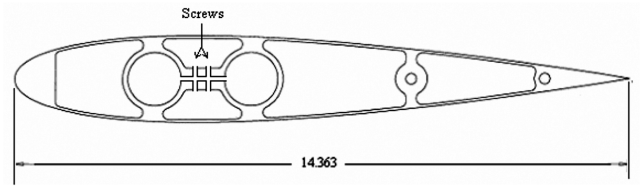

Fig. 13 Middle section rib.

C. Rib Sections Design

The rib sections profiles were chosen to accommodate a double-spar configuration and support the aeroforces. Accordingly, the NACA four-digit series was chosen because it is widely recognized and well understood. Furthermore, a symmetrical airfoil is desirable to facilitate theoretical predictions as well as manufacturing. The smallest airfoil shape was designed using the NACA 0013 base equation and adapting the chord so that the two telescopic spars contour could be contained in the profile. The two larger airfoil shapes were designed to allow an even clearance of 0.060 in.. Figure 12 illustrates the design of the telescopic wing concentric airfoils and displays the location of the spars.

It is relatively easy to cut rib sections out of a 0.25 in. thick aluminum plate using a programmable milling machine. However, each of them had to be manufactured differently so that it could be attached at the right location on the spar. The areas described on Fig. 13, for example, were extruded to make the pieces lighter and provide room for the sensors, electric cables, and pneumatic tubes. The root section rib is slid on the two spars and rests on their attachment piece. The middle section rib was machined so that two screws can be used to tighten and solidly clamp the rib at the tip of the spars' middle section as shown on Fig. 13. The tip rib section was not completely extruded because it faces the exterior of the wing. However, some areas were machined to make it lighter, and two squared pockets were created to fit and attach to the end caps of the spars.

D. Span Sensing and Control System

The control system developed for the pneumatic telescopic wing should minimize the use of moving parts, and should be lightweight and easy to embed into the wing structure. This system should allow a real-time, closed-loop control of the wingspan. Each moving element of the telescopic spar can have an infinite number of positions between its fully extended and retracted states. Thus, a continuous sensing device will be necessary. Note that the fully integrated wing leaves very little space for sensors and wiring, as seen in Fig. 13.

Initially, an opto-electronic distance measuring sensor was chosen because of its simplicity of use and installation. However, the use of this sensor proved to be difficult for several reasons. First, off-the-shelf sensors are very sensitive to the lighting conditions, therefore the lighting conditions have to be consistent from test to test. In addition, because the optic sensor emits a conic group of rays rather than a unique perpendicular ray of light, it was not possible to use the chosen sensor in the confined space within the skin elements. Therefore, linear displacement of the wing sections was sensed using two sets of rack and pinion system, driving a potentiometer. A limited-number-of-turns potentiometer with a linear correlation with distance was used. A rack was mounted inside each of the two moving ribs and was aligned with the pinion-potentiometer set that was solidly mounted onto the lower rib for the two moving wing sections. Consequently, the relative displacement of each section with respect to its lower section was sensed. Figure 14 displays the lower and upper potentiometers attached, respectively, to the root and middle wing sections.

The sensors were calibrated before being included in the control program. The control program, written in Labview, National Instruments, was created to manage the deployment of the wing. The closed-loop control system receives the output voltage from the span displacement sensors through a data acquisition device, and compares it to the command given by the user. Its primary requirement is to be able to sense the instantaneous length of the wing, and respond in a timely manner to a wingspan command given by the user. The control program was able to collect data from the length sensors embedded in the wing, correlate this data in terms of wingspan, and respond to a user's command by managing the opening and closing of solenoid valves to match actual and desired span. The solenoid valves command the input and output of pressure

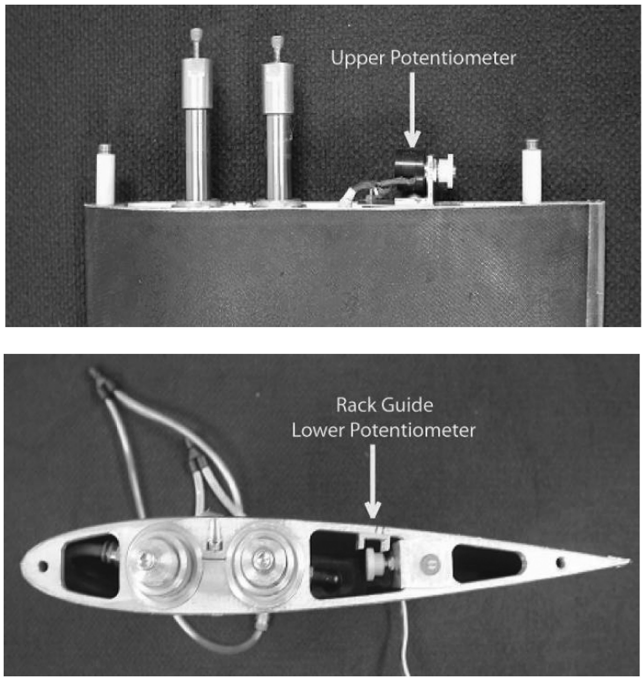

Fig. 14 Length sensor mounted into the wing.

in the actuator to generate its extension or retraction. This is achieved by sending a positive voltage signal to the valves to cause the opening, or a zero voltage signal otherwise (the rest state of the solenoid valves being "closed").

The performance of the control program depends on numerous factors, which influence in a more or less drastic fashion the precision of the controller. These factors are 1) the controller sampling rate; 2) the pneumatic damping effects, resulting from a volume of air being pushed through an orifice; 3) the tolerance on the total length accepted by the control program, which drives directly the overall precision of the controller; 4) the operating pressure for the extension and retraction of the actuator (this parameter defines the amplitude of the pneumatic effects); and 5) the aerodynamic forces supported by the wing, which affects greatly the initial time response.

A general operating rule was to allow for the pneumatic effect to dissipate between actions. This means that a large operating pressure should be matched with a very small controller sampling rate.

Figure 15 presents an example of the control system operation: the top screen displays a distance command sequence given by the user, plotted vs the computer time unit. The bottom screen displays the actual length of the wing given by the length sensors, plotted vs the same time unit. A comparison of these plots highlights the response delay of the spars (the change in length is not instantaneous). In addition, the spar sometime overshoots the desired length before the controller forces it back to the desired position. Finally, notice that the end of the figure a time lag at about midheight, which corresponds to the phenomenon of static friction that prevents the smaller part of the tube from retracting until the required pressure is attained behind the piston and the force is overcome. Finally, the last four teeth of the test point to a time lag at about midheight, which corresponds to a phenomenon of static friction that prevents the smaller part of the tube from retracting until the required pressure is attained behind the piston and the force is overcome.

E. Telescoping Skin Design and Manufacturing

The choice of the wing skin design is an important part of the pneumatic telescopic wing development. Skins must be structurally stiff to maintain the shape of the airfoil and transfer the aerodynamic loads to the wing structure at every stage of the wing deployment or retraction. Two options were studied: the first and more complex option consisted of a soft "foldable" or "rollable" fabric to create the skin. This would allow a very large stroke but would require a rolling

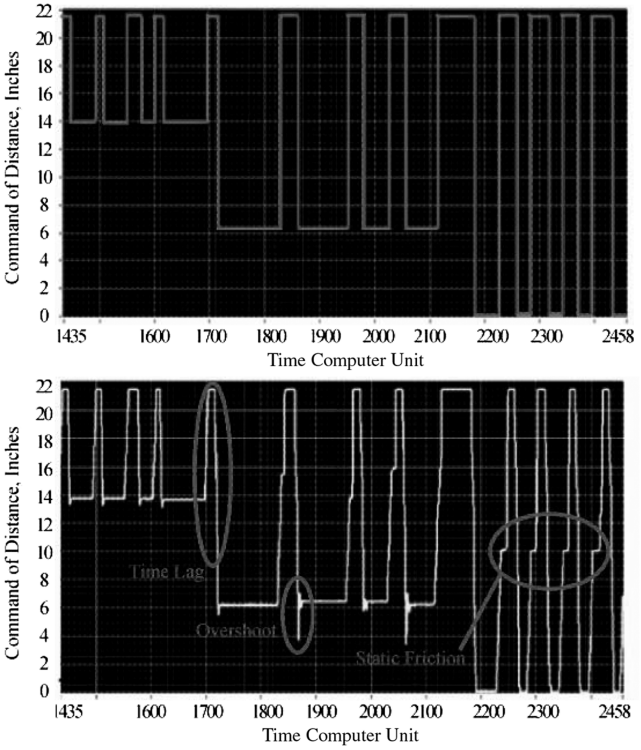

Fig. 15 Control system test example.

and unrolling system or a complex autofolding skin structure. The second option involved the use of hollow shells to create a telescopic skin, which is the most straightforward solution, and the one that was elected.

The manufacturing steps of the hollow skin shells for the telescopic wing prototype are described as follows: First, thin aluminum templates of the dimensions presented earlier in Fig. 12 were cut out of an aluminum plate using a programmable milling machine. Two templates of each size are required to cut airfoils out of styrofoam using hot-wire technology. Once those foam airfoils are cut, they are wrapped with a layer of Teflon paper, two layers of fiberglass, and another layer of Teflon paper. The purpose of Teflon paper is to prevent the fiberglass from sticking to the foam inside and outside mold elements. Additionally, experience showed that two layers are enough to produce a 0.040 in. thin taut shell. At this point, it is critical to verify that the trailing edge of the airfoil is not too long/short, because it can hardly be rectified after curing. The wrapped foam airfoil is then placed back in its foam bed and in a vacuum bag before being cured at 180°F for a minimum of 10 h. Note that every step in the manufacturing process has to be very carefully executed to avoid bumps, wrinkles, and twist of the shell during curing. Also, an inch of span should be added to the airfoil to account for potential melting areas on the edges. The excess can be trimmed after curing. Once the airfoil is cured, the inside foam can be removed by simply pulling on the Teflon paper. Additional steps included sanding and surface coating to ensure smoothness of the shell's surface. During every operation it was important to keep the foam core inside the shell to make sure the structure of the fibers was not damaged. Figures 16–18 present details of the integrated pneumatic telescopic wing assembly.

III. Pneumatic Telescopic Wing Aerodynamic Performance

A. Test and Prototype Setup

To compare the test data to theoretical aerodynamic results, lift and induced drag theoretical values were calculated using the panel airfoil program X-Foil.[‡] The parasite drag values for the telescopic

[‡]Data available online at http://raphael.mit.edu/xfoil [retrieved May 2004].

Fig. 16 Integrated wing assembly: pneumatic spars and root rib.

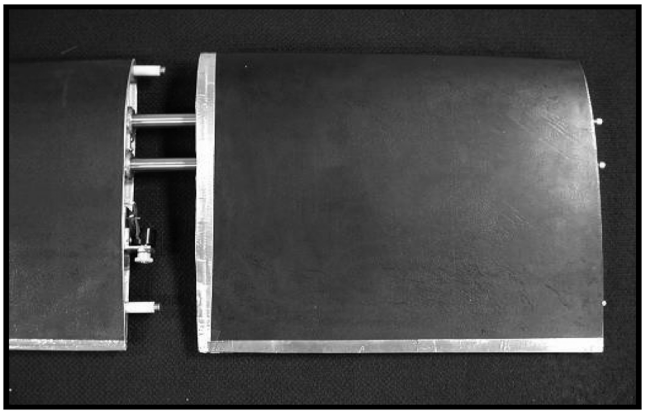

Fig. 17 Integrated wing assembly: tip skin element, potentiometer.

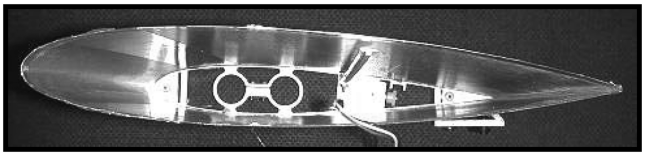

Fig. 18 Integrated wing assembly: middle skin (pinion, rack, rib).

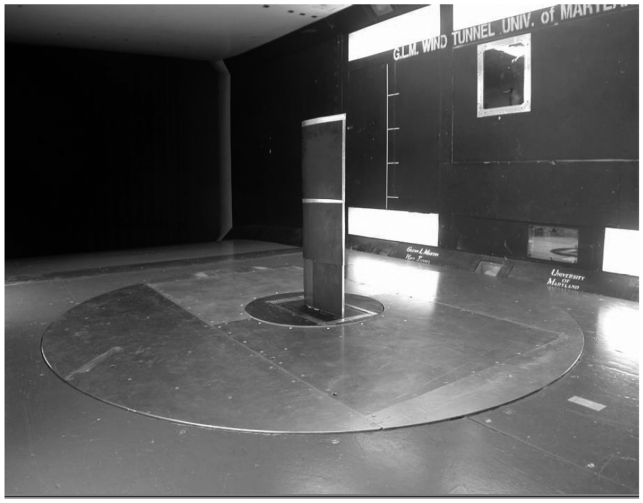

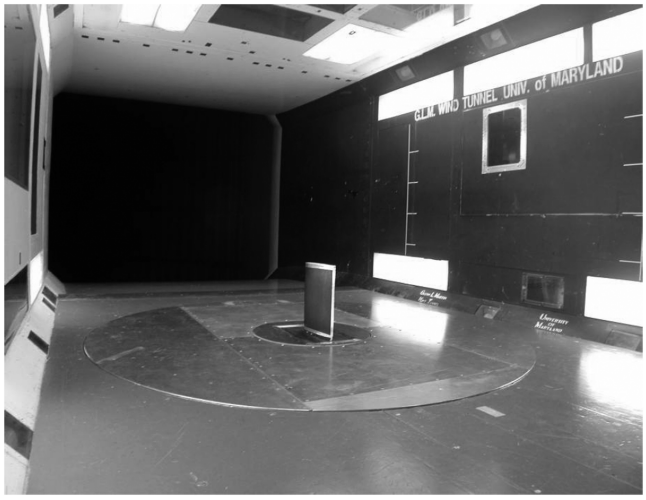

Fig. 19 Pneumatic telescopic wing mounted in the Glenn L. Martin Wind Tunnel in extended and retracted configurations.

wing prototype are shown in Table 1. The values obtained did not account for the wing aspect ratio and were only dependent on the airfoil geometry and the Reynolds number. The sets of parasite drag values obtained seemed to diverge drastically above a 14-deg angle of attack; therefore a constant value of parasite drag, equal to the 14 deg value, was set above this angle, as shown in Table 1.

Wind-tunnel tests of the full-scale wing were conducted at the Glenn L. Martin Wind Tunnel facility at the University of Maryland in March and July 2004. The test section is 7.75 ft high by 11.04 ft wide, and the flow speed ranges from 2 to 230 mph (i.e., from $M = 0.0$ to $M = 0.3$). The experiments were conducted on a six-component yoke-type balance with an error of 0.001 lb on the lift and drag values The wing was mounted vertically on the floating wind-tunnel floor, which is directly mounted on the balance, as shown in Fig. 19. All forces and moments were measured and the aerodynamic center of the wing was aligned with the center of the balance to simplify the interpretation of the wind-tunnel data.

The telescopic wing was tested at three freestream velocities (20, 25, and 30 mph), thus Reynolds numbers (227,390, 284,290, and 341,120), at four different spans (40, 60, 80, and 100%), and for an angle of attack varying from 0 to after stall (estimated between 18 and 24 deg). Additionally, two foam-core/fiberglass solid wings, of spans corresponding to the fully retracted (40%) and fully extended (100%) telescopic wing configurations, were tested to verify the order of

Table 1 Parasite drag coefficients for given Reynolds numbers

α, deg	$V_\infty = 20$ mph	$V_\infty = 25$ mph	$V_\infty = 35$ mph
	$Re = 227,390$	$Re = 284,390$	$Re = 341,120$
	C_{Dp}	C_{Dp}	C_{Dp}
0	0.00937	0.00818	0.00749
1	0.01043	0.00921	0.00841
2	0.0119	0.0111	0.01039
3	0.01442	0.01351	0.01286
4	0.01905	0.01743	0.01637
5	0.02539	0.02312	0.02164
6	0.03556	0.03165	0.02858
7	0.05362	0.04543	0.04126
8	0.18305	0.08646	0.0688
10	0.19871	0.15882	0.09927
12	0.21137	0.16943	0.21067
14	0.22773	0.17996	0.22119
16	0.24151	0.19189	0.23926
17	0.25486	0.20275	0.25448
18	0.26912	0.21363	0.26612
19	0.28107	0.22525	0.28158
20	0.29517	0.23631	0.2925
21	0.00937	0.00818	0.00749
22	0.01043	0.00921	0.00841
23	0.0119	0.0111	0.01039
24	0.01442	0.01351	0.01286

Table 2 Test matrix of angles of attack for given Reynolds number and wingspan configuration

V_∞	Re	Wingspan			
		16.5 in.	23.1 in.	30.8 in.	38.5 in.
20 mph	227,390	0–24 deg	0–24 deg	0–24 deg	0–24 deg
25 mph	227,390	0–24 deg	0–24 deg	0–24 deg	0–24 deg
30 mph	227,390	0–24 deg	0–24 deg	0–24 deg	0–24 deg

magnitude of the forces and aerodynamic results. The test matrix for the telescopic and solid wings is shown in Table 2.

The main airfoil section was NACA 0013-based, with a chord of 14.625 in. The wingspan varied between 16.5 and 38.5 in. Seams were reduced at the changes of airfoil section using an aluminum lip. Considering the wind-tunnel results of a previous design [5] (stiff hollow telescopic skin elements), and that the aerodynamic performance should be improved after reducing the seams, the experimental maximum lift-to-drag ratio was expected to be between 85 and 90% of the theoretical result for all of the three wingspans considered.

B. Aerodynamics Results

Figures 20–25 show lift coefficient C_L, drag coefficient C_D, and lift-to-drag ratio L/D for the telescopic wing in its retracted configuration (40% of maximum span) then in its fully extended configuration (100% of maximum span). The plots also show theoretical predictions and data collected for the solid wing. Although the following results are only presented for a wind speed of 20 mph, or a Reynolds number of 227,390, the same trends were observed very consistently at the other test speeds (25 and 30 mph).

The lift curves, in both configurations, displayed good agreement between the three cases (telescopic wing, finite wing theory, and

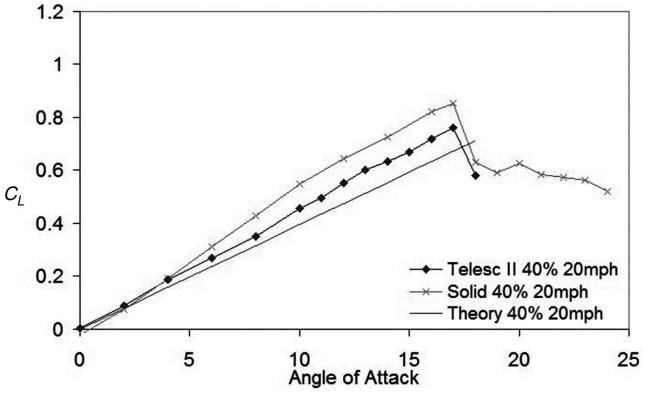

Fig. 20 Lift coefficient vs angle of attack in retracted configurations at $Re = 227,390$ (20 mph).

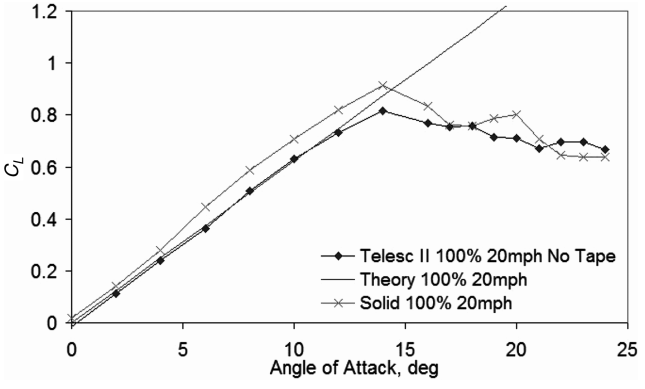

Fig. 21 Lift coefficient vs angle of attack in extended configurations at $Re = 227,390$ (20 mph).

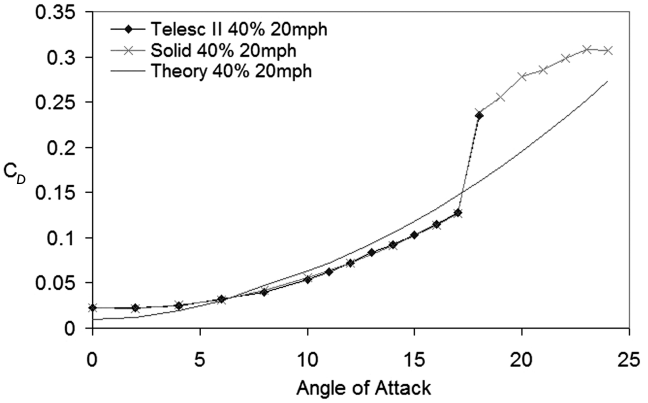

Fig. 22 Drag coefficient vs angle of attack in retracted configurations at $Re = 227,390$ (20 mph).

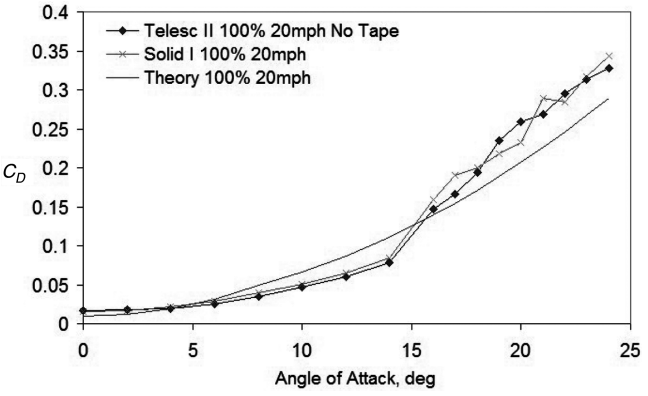

Fig. 23 Drag coefficient vs angle of attack in extended configurations at $Re = 227,390$ (20 mph).

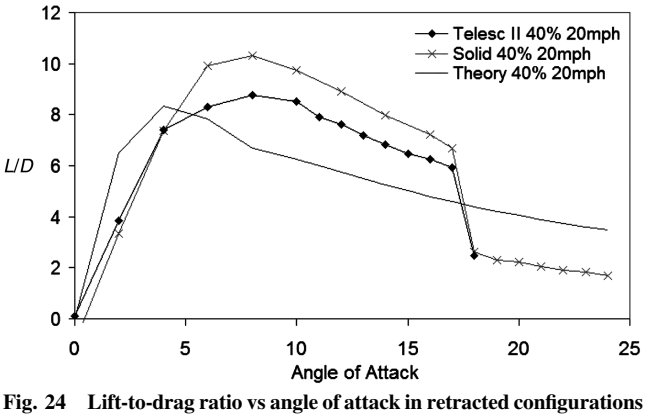

Fig. 24 Lift-to-drag ratio vs angle of attack in retracted configurations at $Re = 227,390$ (20 mph).

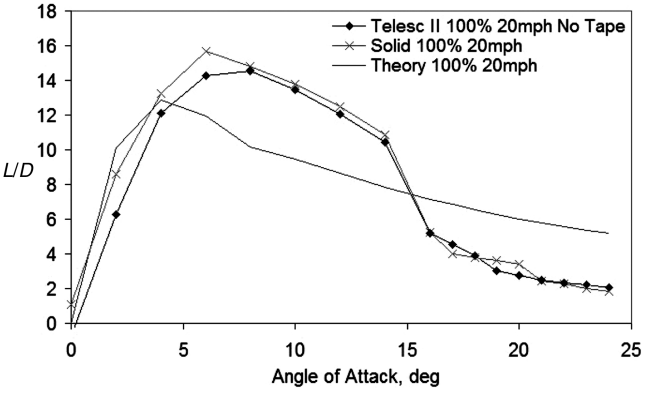

Fig. 25 Lift-to-drag ratio vs angle of attack in extended configurations at $Re = 227,390$ (20 mph).

Table 3 Comparison of the maximum lift-to-drag ratios at two different speeds (or Reynolds numbers)

Max L/D	40% of maximum span		100% of maximum span	
	20 mph	30 mph	20 mph	30 mph
Telescopic wing	9 ($\alpha = 8$ deg)	9 ($\alpha = 8$ deg)	14.4 ($\alpha = 6$ deg)	14.6 ($\alpha = 6$ deg)
Finite wing theory	8.5 ($\alpha = 4$ deg)	9.5 ($\alpha = 4$ deg)	13 ($\alpha = 4$ deg)	14 ($\alpha = 4$ deg)
Solid wing	10.5 ($\alpha = 8$ deg)	11 ($\alpha = 6$ deg)	15.8 ($\alpha = 8$ deg)	16.2 ($\alpha = 6$ deg)

Table 4 Extension and retraction pressures under aerodynamic load

α	$V_\infty = 20$ mph		$V_\infty = 30$ mph	
	Extension pressure	Retraction pressure	Extension pressure	Retraction pressure
0 deg	25 psi	40 psi	30 psi	40 psi
5 deg	25 psi	40 psi	30 psi	40 psi
10 deg	25 psi	40 psi	30 psi	45 psi
15 deg	25 psi	45 psi	30 psi	45 psi
18 deg	25 psi	45 psi	30 psi	45 psi

solid wing), even though the theoretical curves were slightly lower than the two experimental curves. However, in both cases the solid wing displayed a slightly higher value of lift as illustrated in Figs. 20 and 21. The drag curves were in good agreement for both the extended and retracted configurations (Figs. 22 and 23). The solid wing appeared to generate slightly more lift than the telescopic wing at higher speeds. In addition, at high wingspans (100%) the behavior of the telescopic wing and the solid wing differed near stall conditions. This trend was observed consistently at other test speeds (25 and 30 mph). The theoretical value of drag being strongly dependent on the induced drag, which is a function of the theoretical lift, does not show an abrupt change at the stall angle, but overall the experimental curves match fairly well with the theoretical analysis.

The flexibility of the telescopic skins observed during testing could potentially play a role in the small discrepancies in lift and drag values for the telescopic wing. As the angle of attack increases, the lower and upper surfaces of the airfoil may be deformed by external pressure, changing the overall profile of the wing. This would result in a cambered airfoil that would be expected to produce more lift for the same amount of drag at a given angle of attack, when compared to a symmetric airfoil of similar thickness distribution. For instance, this would be the result expected if a NACA 2413 and a NACA 0013 were compared [9]. In addition, this change in the airfoil section should be accompanied by a delay in stall. However, these expected trends do not agree with the trends observed in the experimental results because lift is actually reduced for the telescopic wing, whereas the drag remains effectively unchanged. Several factors observed during testing might be a cause for these unexpected trends. First, an air leakage from the lower to the upper surface of the wing through the seams was observed. This leakage may reduce the difference in pressure between the upper and lower surfaces of the wing, resulting in a loss of lift and potentially a disturbance of the flow over the upper surface of the wing. Secondly, the seams between telescopic skin elements created a discontinuity of the wing surface. This geometric discontinuity will be studied in the next section of this paper.

The differences in lift and drag properties of the telescopic and solid wing appear minor, but are more pronounced when one examines the lift-to-drag ratio plots (Figs. 24 and 25). In the retracted configuration (40% of the maximum span), the telescopic wing underperforms the solid wing curve by 14% peak to peak. In the extended configuration, the telescopic wing underperforms the solid curve by about 9% peak to peak. This can be justified by the lower stiffness of the surface for the telescopic wing, and in the extended case the seams at the junction of the telescopic wing skin element are apparent. This effect will be studied in the next section.

These conclusions are based on a very good repeatability of the aerodynamic results throughout a range of wingspan going from 40 to 100%, and a range of speeds going from 20 to 30 mph. Table 3 presents the maximum lift-to-drag ratio values for both the extended and retracted configuration, and at the lowest and highest test speeds.

Finally, the wing was deployed in the wind at different angles of attack to identify the pressures required to actuate the wing under aerodynamic loads in both directions. (Table 4 presents the results of this analysis.) This systematic characterization of the telescopic wing proves that it can be extended and retracted under aerodynamic loads with pressures as low as 25 psi at low speeds. The retraction pressures are consistently lower than the extension pressures. This is expected because the force required to push a piston is proportional to its surface, and the retraction surfaces are smaller than the extension surfaces on the pistons.

C. Impact of the Seams on the Aerodynamic Performance

As mentioned in the preceding section, the seams between telescopic skin elements create a geometric discontinuity on the wing surface, highlighted in Fig. 26.

The impact of this geometric discontinuity on the aerodynamic performance of the wing was studied by investigating the performance of the telescopic wing with the seams covered using thin aluminum foil tape to seal the seams in a static study. The results of this test were then compared to that of the original telescopic wing with open seams. The results are compared in Figs. 27–29.

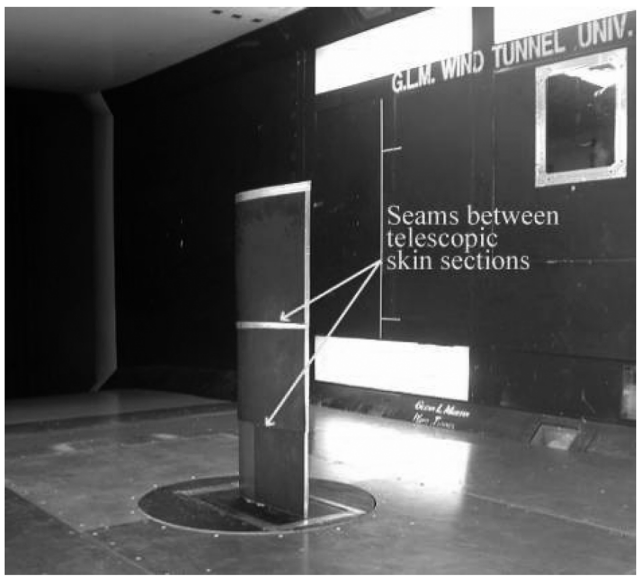

Fig. 26 Seams between telescopic skin sections.

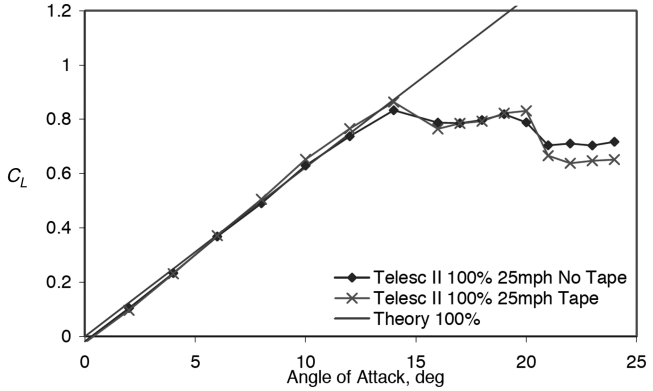

Fig. 27 Comparison of lift coefficients for the telescopic wing model, at 100% span and 25 mph: impact of the seams.

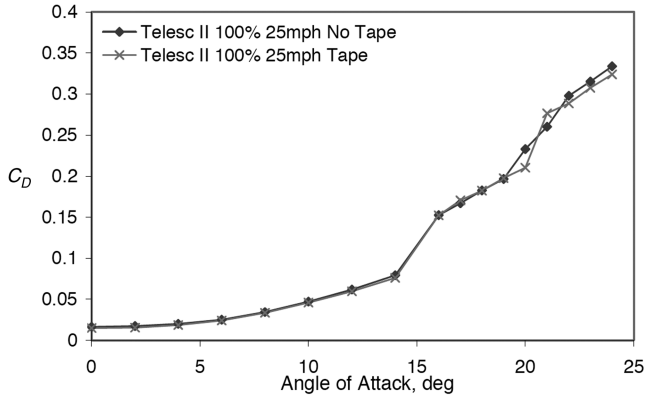

Fig. 28 Comparison of drag coefficients for the telescopic wing model, at 100% span and 25 mph: impact of the seams.

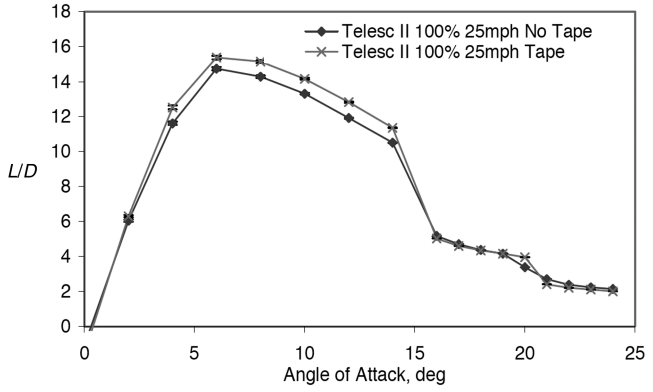

Fig. 29 Comparison of lift-to-drag ratios for the telescopic wing model, at 100% span and 25 mph: impact of the seams.

Covering the seams between two telescopic skin elements affects lift values, whereas the drag values remain effectively unchanged. At the scale of the plot, the lift and drag curves for the "tape" and "no tape" cases appear to be very close together, and the error on the data (0.001 lb for the lift and drag values) tends to be much smaller than the difference between the two curves at a given angle of attack. But even a small difference in the lift and drag coefficients actually results in a more significant difference in the L/D curves.

In addition, propagation of the error on the lift curves and the drag curves results in visible error bars on the L/D curve. Figure 29 displays the L/D ratio for the tape and no tape cases: although error bars are visible at the scale of the plot, the error at a given angle of attack is much smaller than the difference between the two cases. This study of the error confirms that the difference between the two

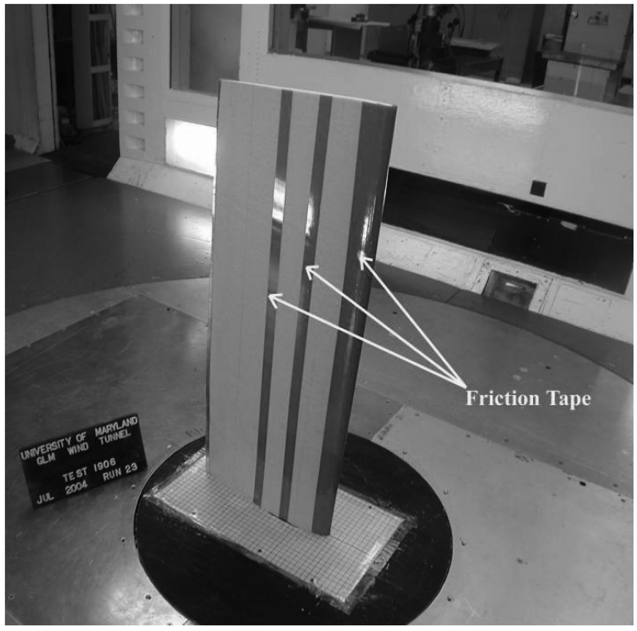

Fig. 30 Friction tape along the span of the solid wing: 100% wingspan.

cases does not fall within the range of experimental error and thus confirms the validity of the trend observed throughout all data sets: when the seams are covered, lift is improved consistently and even more so when the airfoil approached stalls. Although only one of the cases is represented here (25 mph, fully extended wing), the behavior observed is very consistent throughout all the data sets collected (three different speeds and three different wingspans). The lift-to-drag ratio can be improved by up to 10% for certain wingspan at higher speed (60% wingspan at 30 mph). Hence, a next-generation pneumatic telescopic wing should include devices to keep the seams sealed at all times.

D. Impact of the Friction Tape on the Aerodynamic Performance

To reduce friction of the telescopic skins onto each other, particularly at the leading edge, and facilitate the deployment/retraction of the pneumatic telescopic wing, a very smooth surface tape (friction tape) was laid along the span of the telescopic wing. Because the friction tape was located in an area where the boundary layer should be and remain attached (highlighted in Fig. 30), a comparison study was conducted to identify its impact on the aerodynamic performance.

To identify the effect of the friction tape on the performance of the models, the solid wing was tested in the wind tunnel with friction tape laid spanwise on its surface, in the same pattern as the telescopic wing. Then the tape was removed and the tests were repeated. Figures 31–33 present the results of this test.

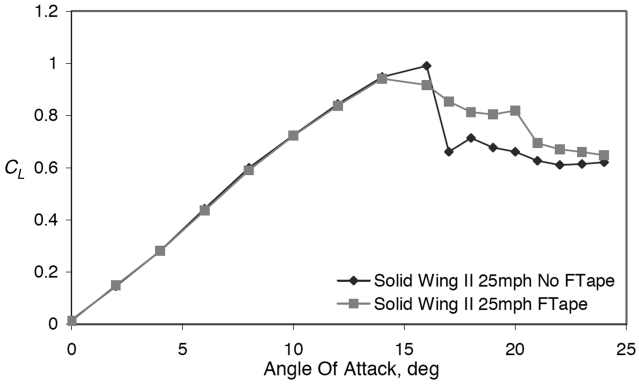

Fig. 31 Comparison of lift coefficients for solid wing model, at 100% span and 25 mph: impact of the friction tape.

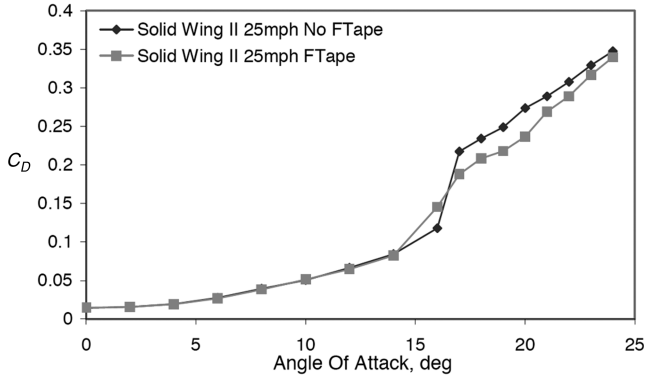

Fig. 32 Comparison of drag coefficients for solid wing model, at 100% span and 25 mph: impact of the friction tape.

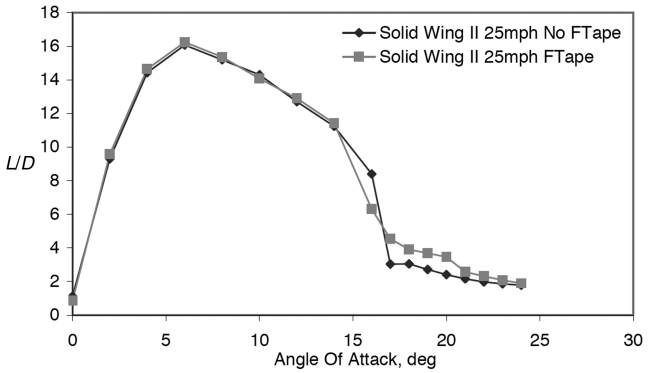

Fig. 33 Comparison of lift-to-drag ratios for solid wing model, at 100% span and 25 mph: impact of the friction tape.

The lift curves are really close together all the way to stall. It appears consistently (the same results is observed at 20 and 30 mph) that the wing stalls earlier when it wears friction tape on its surface. As a result, drag is also slightly different when the angle of attack approached 14 deg. Thus, the lift-to-drag ratios are almost identical whether the wing is outfitted with friction tape or not. This gives us an indication that the performance of the telescopic wing should not be affected by the presence of the friction tape on its surface. This experiment was repeated with a solid wing of 40% wingspan and the results were consistent, showing that the presence of the friction tape along the span of the wing has virtually no effect on aerodynamics performance.

IV. Conclusions

Morphing wing technologies have been used on manned aircraft over the years, but never on a UAV. Morphing the wing geometry enhances not only the aerodynamic performance, but also the aircraft maneuverability. This allows a single aircraft to perform various missions. This paper considers the design, development, and testing of a pneumatic telescopic wing. Key elements of the wing consist of a pneumatic telescopic spar, rigid airfoil skins, and rib elements. The telescopic wing assembly has the ability to undergo a 230% change in aspect ratio while supporting aerodynamic loads. Preliminary structural analysis suggests that this wing concept can be used in a small-scale UAV. Wind-tunnel tests were conducted in the Glenn L. Martin Wind Tunnel at the University of Maryland in March and July 2004. Data from these tests were compared to the theoretical results and confirm that the aerodynamic performance of the telescopic wing suffers slightly of parasitic drag created by the seams of the wing sections and of a softer skin. Nevertheless, in its fully deployed condition the telescopic wing can achieve lift-to-drag ratios as high as 16, which is as high as its solid foam-core wing counterpart. In addition, the wing can be deployed and retracted under aerodynamic load, up to stall and beyond, with actuation pressures as low as 25 and 45 psi.

Future work will involve improvement of the manufacturing techniques to provide stiffer and geometrically perfect telescopic skins to guarantee that bending does not cause extra friction during deployment. Fairings will also be developed to seal the seams between telescopic skins at all stages of deployment or retraction of the spars. Future work will also involve the determination of the stability and control characteristics as well as the aeroelastic properties of the pneumatic telescopic wing. Ultimately, it is expected that pneumatic telescopic wings can be mounted on a UAV to provide roll control. Recent theoretical study of variable wingspan wing shows advantages such as drag reduction range increase and good roll motion control [10].

Appendix: Strain and Moment Derivations

I. Root Moment Derivation

A. Integration Formulas Used

$$\int \sqrt{a^2 - X^2}\,\mathrm{d}X = \frac{X}{2}\sqrt{a^2 - X^2} + \frac{a^2}{2}\sin^{-1}\left(\frac{X}{a}\right)$$

$$\int X\sqrt{a^2 - X^2}\,\mathrm{d}X = -\frac{1}{3}(a^2 - X^2)^{3/2}$$

$$\int \frac{\mathrm{d}X}{\sin(AX)} = \frac{1}{A}\ell_n\left[\tan\left(\frac{AX}{2}\right)\right]$$

B. Lift Distribution and Constants

$$q(X) = \rho_\infty V_\infty \Gamma_o \sqrt{1 - \left(\frac{2X}{b}\right)^2} = C_1\sqrt{C_2}\sqrt{a - X^2}$$

$$C_1 = \rho_\infty V_\infty \Gamma_o \qquad C_2 = \frac{4}{b^2} \qquad a = \frac{1}{\sqrt{C_2}} \qquad A = \frac{1}{a}$$

II. Strain and Moment Derivation

$$\frac{\mathrm{d}V}{\mathrm{d}X} = -q(X) \quad \text{and} \quad \frac{\mathrm{d}M}{\mathrm{d}X} = V$$

III. Strain Derivation and Boundary Condition

$$-V(X) = \int q(X)\,\mathrm{d}X = C_1\sqrt{C_2}\left[\frac{X}{2}\sqrt{a^2 - X^2} + \frac{a}{2}\sin^{-1}\left(\frac{X}{a}\right)\right] + D_1$$

$$V(0) = 0 \Rightarrow D_1 = C_1\sqrt{C_2}\left[\frac{X}{2}\sqrt{a^2 - X^2} + \frac{a}{2}\sin^{-1}\left(\frac{X}{a}\right)\right]$$

IV. Moment Derivation and Boundary Conditions

$$M(X) = \int V(X)\,\mathrm{d}X = -\frac{C_1\sqrt{C_2}}{2}[-(a^2 - X^2)^{3/2}] - \frac{C_1\sqrt{C_2}}{2}a^2\left[\frac{1}{A}\ell_n\left(\tan\frac{AX}{2}\right)\right] - D_1X + D_2$$

$$M(L) = 0 \Rightarrow D_2 = \frac{C_1\sqrt{C_2}}{2}[-(a^2 - L^2)^{3/2}] + \frac{C_1\sqrt{C_2}}{2}a^2\left[\frac{1}{A}\ell_n\left(\tan\frac{AL}{2}\right)\right] + D_1L$$

V. Root Moment

$$M(0) = -\frac{C_1\sqrt{C_2}}{2}\left[-\frac{1}{3}(a^2)^{3/2}\right] + 0 - 0 + D_2$$

$$M(0) = -\frac{C_1\sqrt{C_2}}{2}\left[-\frac{1}{3}(a^2)^{3/2}\right] + \frac{C_1\sqrt{C_2}}{2}[-(a^2 - L^2)^{3/2}] + \frac{C_1\sqrt{C_2}}{2}a^2\left[\frac{1}{A}\ell_n\left(\tan\frac{AL}{2}\right)\right] + L\left\{C_1\sqrt{C_2}\left[\frac{X}{2}\sqrt{a^2 - X^2} + \frac{a}{2}\sin^{-1}\left(\frac{X}{a}\right)\right]\right\}$$

Acknowledgments

The authors would like to thank Bernie LaFrance, Janisa Henry, Justin Richeson, and Paul D. Samuel for their assistance on various parts of this project. In addition, the authors would like to thank Ergo-Help, Inc., for assisting with the design and manufacturing of the telescopic spars.

References

[1] Gallington, R. W., Berman, H., Entzminger, J., Francis, M. S., Palmore, P., and Stratakes, J., "Unmanned Aerial Vehicles," *Future Aeronautical and Space Systems*, AIAA, Reston, VA, 1997, pp. 251–296.

[2] Hayden, K. L., "Aircraft Wing Construction," U.S. Patent 2,056,188, 1936.

[3] Sarh, B., "Convertible Fixed Wing Aircraft," U.S. Patent 4,986,493, 1990.

[4] Lin, J., Cadogan, D., Huang, J., and Feria, V. A., "An Inflatable Microstrip Reflect-Array Concept for Ka-Band Applications," AIAA Paper 2000-1831, April 2000.

[5] Blondeau, J. E., Richeson, J., and Pines, D. J., "Design, Development and Testing of a Morphing Aspect Ratio Wing Using an Inflatable Telescopic Spar," AIAA Paper 2003-1718, April 2003.

[6] Blondeau, J. E., and Pines, D. J., "Wind Tunnel Testing of a Morphing Aspect Ratio Wing Using a Pneumatic Telescopic Spar," AIAA Paper 2003-6659, Sept. 2003.

[7] Blondeau, J., and Pines, D., "Pneumatic Morphing Aspect Ratio Wing," AIAA Paper 2004-1808, 2004.

[8] Anderson, J. D., Jr., *Fundamental of Aerodynamics*, 2nd ed., McGraw–Hill, New York, 2001.

[9] Abbott, I. H., and Von Doenhoff, A. E., *Theory of Wing Sections*, McGraw–Hill, New York, 1959, pp. 462–463, 478–479.

[10] Bae, J., Seigler, T., Inman, D., and Lee, I., "Aerodynamic and Aeroelastic Considerations of a Variable-Span Morphing Wing," AIAA Paper 2004-1726, 2004.